IMPLEMENTATION OF CLOUD MICROPHYSICS IN THE CSU GCM

Laura D. Fowler and David A. Randall
Department of Atmospheric Science
Colorado State University
Fort Collins, Colorado, USA

1. INTRODUCTION

Clouds are one of the key climate-system components affecting the dynamics of the atmosphere through complex couplings among radiative, thermodynamic, and dynamic processes (Arakawa, 1975). Interactions between clouds and radiation and between clouds and the hydrological cycle are inadequately understood. Realistic parameterizations of these interactions in terms of cloud microphysical processes and cloud radiative properties are only now being developed for use in atmospheric general circulation models (GCMs). Such parameterizations are needed in order to assess the effects of clouds on climate, especially in the context of climate change studies.

Microphysical processes responsible for the formation and dissipation of water and ice clouds have been incorporated into the Colorado State University General Circulation Model in order to: (1) yield a more physically based representation of the components of the atmospheric moisture budget; (2) link the distribution and optical properties of the model-generated clouds to the predicted cloud water and ice amounts; and (3) produce more realistic simulations of the cloudiness and the Earth's radiation budget.

The purpose of the present paper is to provide a short description of the cloud microphysics parameterization, and the simulated hydrological cycle and top-of-the atmosphere radiation budget. The sensitivity of the simulated climate to several key parameters of the cloud microphysics scheme is discussed. Results are presented using a full annual cycle simulation, as well as 120-day sensitivity experiments for perpetual January conditions.

2. CLOUD MICROPHYSICS

Our cloud microphysics parameterization is based on the bulk cloud microphysics equations developed for mesoscale cloud models as described by Lin et al. (1983), and Rutledge and Hobbs (1983, 1984). We introduce five prognostic moisture variables for the mixing ratios of water vapor, cloud water, cloud ice, rain, and snow. Cloud water and cloud ice are predicted to form through large-scale condensation and deposition processes. An important additional source of cloud water and cloud ice is detrainment at the tops of cumulus towers. We assume that the fallspeeds of cloud water and cloud ice particles are negligible. Rain and snow, of course, have non-negligible fall velocities.

At present, our cloud microphysics parameterization does not include a prognostic equation for the number concentration of cloud water droplets and cloud ice crystals. This simplification allows us to express the rate

of condensation of water vapor to cloud water and the rate of deposition of water vapor to cloud ice as a function of the large-scale supersaturation. In so doing, we do not distinguish between homogeneous and heterogeneous nucleation for the ice phase. We assume that there always exist sufficient nuclei to initiate condensation and deposition.

Water vapor is a source of cloud water (PCOND) and cloud ice (PSUB). Cloud water is assumed to form by condensation when the temperature (T) is greater than or equal to $T_0 = 0^oC$ and the air is supersaturated with respect to water. Cloud ice is predicted to form by deposition of vapor if $T < T_{00}$ and the air is supersaturated with respect to ice. Supercooled cloud water and cloud ice are allowed to coexist in the temperature range $T_{00} \leq T < T_0$ (PBERG). Here, we choose $T_{00} = -20^oC$. Water vapor can also be converted to rain and snow by condensation (PREVP) and deposition (PSEVP), respectively.

Cloud water is a source for water vapor through evaporation in a subsaturated layer (PCOND), or a source of rain if the air remains supersaturated. The conversion of cloud water to rain occurs through two different mechanisms: (1) autoconversion of cloud water to rain (PRAUT); and (2) collection of cloud water by rain (PRACW). Supercooled cloud water is also a source for snow by riming (PSACW), and it can be a source of cloud ice through the Bergeron process $(T_{00} \leq T < T_0)$, or instantaneous freezing $(T < T_{00})$.

Cloud ice is a source of water vapor by sublimation when the air is subsaturated with respect to ice (PSUB). Otherwise, cloud ice is a source for snow through two different mechanisms: (1) autoconversion of cloud ice to form snow (PSAUT); and (2) collection of cloud ice by snow (PSACI). Instantaneous melting of cloud ice to form cloud water occurs if $T \geq T_0$ (PSMLTI).

Rain is a source for water vapor by evaporation (PREVP). Rain may also be a source for snow by instantaneous freezing if $T < T_0$ (PSMLTS). Snow is a source for water vapor by sublimation (PSEVP). Also, snow may be a source of rain by instantaneous melting (PSMLTS) as it falls through the 0°C level.

Microphysical interactions among water vapor, cloud water, cloud ice, rain, and snow are presented schematically in Fig.1. Acronyms that we have adopted for short names for the various microphysical processes are listed in Table 1. A detailed description of the bulk cloud microphysics equations, including the fallspeed formulation is given in Fowler et al. (1995).

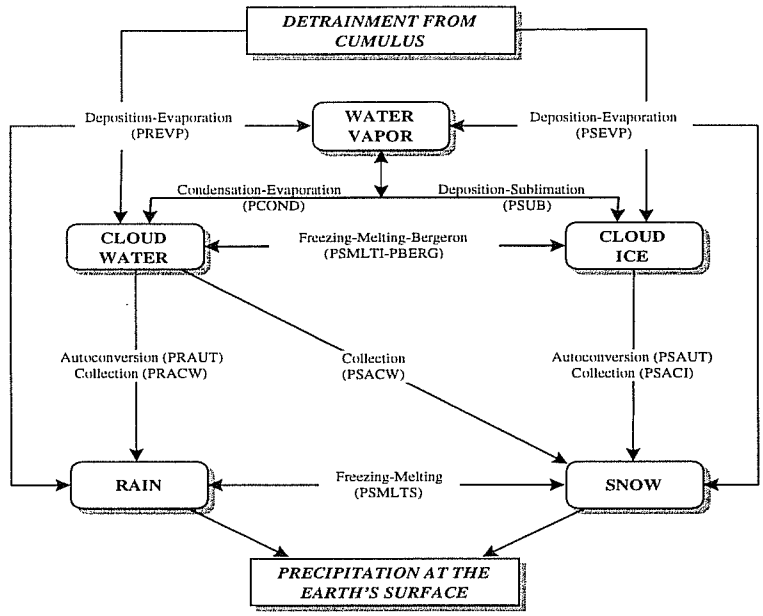

Fig. 1. Schematic diagram of cloud microphysics processes.

Table 1: Keys to Fig. 1.

SYMBOL	MICROPHYSICAL PROCESS
PBERG	Bergeron process
PCOND	Condensation/Evaporation of water vapor
PRACW	Collection of cloud water by rain
PRAUT	Autoconversion of cloud water to rain
PREVP	Deposition of water vapor on rain/Evaporation of rain
PSACI	Collection of cloud ice by snow
PSACW	Collection of supercooled cloud water by snow
PSAUT	Autoconversion of cloud ice to snow
PSEVP	Deposition of water vapor on snow/Evaporation of snow
PSMLTI	Melting of cloud ice
PSMLTS	Melting of snow

2.1 Continuity equations

The CSU GCM uses a modified σ-coordinate (Suarez et al., 1983) to represent the vertical discretization of the atmosphere. Continuity equations for the mixing ratios of water vapor (q_v), cloud water (q_c), cloud ice (q_i), rain (q_r), and snow (q_s), and the potential temperature (θ) on a σ-surface may be respectively written as follows:

$$\frac{\partial}{\partial t}(\pi^* q_v) + \nabla \cdot (\pi^* \mathbf{V} q_v) + \frac{\partial}{\partial \sigma}(\pi^* \dot{\sigma} q_v) = \pi^* (SCM_v + SCUP_v + SCMADJ_v + SDADJ_v + STB_v) , \quad (1)$$

$$\frac{\partial}{\partial t}(\pi^* q_c) + \nabla \cdot (\pi^* \mathbf{V} q_c) + \frac{\partial}{\partial \sigma}(\pi^* \dot{\sigma} q_c) = \pi^* (SCM_c + SCUP_c) , \quad (2)$$

$$\frac{\partial}{\partial t}(\pi^* q_r) + \nabla \cdot (\pi^* \mathbf{V} q_r) + \frac{\partial}{\partial \sigma}(\pi^* \dot{\sigma} q_r) = \pi^* \left[SCM_r + SCUP_r + g \frac{1}{\pi^*} \frac{\partial}{\partial \sigma} (\rho V_r q_r) \right] , \quad (3)$$

$$\frac{\partial}{\partial t}(\pi^* q_i) + \nabla \cdot (\pi^* \mathbf{V} q_i) + \frac{\partial}{\partial \sigma}(\pi^* \dot{\sigma} q_i) = \pi^* (SCM_i + SCUP_i) , \quad (4)$$

$$\frac{\partial}{\partial t}(\pi^* q_s) + \nabla \cdot (\pi^* \mathbf{V} q_s) + \frac{\partial}{\partial \sigma}(\pi^* \dot{\sigma} q_s) = \pi^* \left[SCM_s + SCUP_s + g \frac{1}{\pi^*} \frac{\partial}{\partial \sigma} (\rho V_s q_s) \right] , \quad (5)$$

and

$$\frac{\partial}{\partial t}(\pi^* \theta) + \nabla \cdot (\pi^* \mathbf{V} \theta) + \frac{\partial}{\partial \sigma}(\pi^* \dot{\sigma} \theta) = \pi^* \frac{\theta}{c_p T} (SCM_T + SCUP_T + SCMADJ_T + SDADJ_T + STB_T + SRAD_T) . \quad (6)$$

In (1)-(6), $\nabla \cdot ( )$ denotes the operator on a σ–surface, π^* is the pressure scale used with the definition of σ (see Suarez et al. 1983), $\mathbf{V}$ is the horizontal wind vector, $\dot{\sigma}$ is the vertical velocity and g is the gravitational acceleration. SCM_x, $SCUP_x$, $SCMADJ_x$, $SDADJ_x$, STB_x, and $SRAD_x$ represent[1] the rates of change in q_x and θ due to cloud microphysical processes, cumulus convection, moist convective adjustment, dry convective adjustment, turbulent mixing, and radiation processes, respectively. In (3) and (5), $g \frac{1}{\pi^*} \frac{\partial}{\partial \sigma} (\rho V_x q_x)$ represents the vertical divergence of rain or snow with fallspeed V_x. $SCUP_r$ and $SCUP_s$ are set equal to zero because we assume that condensed water may only be detrained in the form of cloud water and cloud ice.

Fowler et al. (1995) describe in detail the implicit scheme used to predict q_v, q_c, q_r, q_i, q_s, and θ for water clouds ($T \geq T_0$) mixed-phase clouds ($T_{00} \leq T < T_0$), and ice clouds ($T < T_{00}$). It can be shown that, for sin-

1. Here x refers to the subscripts v, c, r, i, s, and T.

gle-phase clouds, the system of equations reduces to four equations for the four unknowns q_v, q_c, q_r, and T for the water phase, and q_v, q_i, q_s, and T for the ice phase. For mixed-phase clouds, i.e. when supercooled cloud water and cloud ice coexist, the system reduces to five equations with the five unknowns q_v, q_c, q_i, q_r, q_s, and T.

The cloud microphysics scheme is applied to model layers located above the PBL, up to 100 mb. We have chosen not to include PBL clouds in the framework of our microphysics parameterization at this time. The reason is that we are in the midst of a complete overhaul of our boundary-layer parameterization, not only changing the boundary-layer clouds but also eliminating the "mixed-layer" assumption (Randall et al., 1992) and revising the entrainment parameterization. We have therefore decided to revise the boundary-layer clouds as part of "Phase 2" of the development of our cloud microphysics parameterization.

Cloud water, cloud ice, rain, and snow are advected using a fourth-order advection scheme. With the current model's coarse resolution, advective processes have a small effect on the global distributions of the moisture budget components, but they must be included to ensure conservation of total water mass. In higher-resolution models these terms will become important.

2.2 Bergeron-Findeisen mechanism

The Bergeron-Findeisen mechanism (Bergeron, 1935) is a microphysical process that favors the growth of cloud ice at the expense of cloud water, and leads to enhanced precipitation due to collection of cloud water by snow when cloud ice, cloud water, and snow coexist in a cloud. This process occurs because the saturation vapor pressure with respect to ice (e_{si}) is less than that with respect to water (e_{sw}). It is most effective at about -12°C, where the difference between e_{sw} and e_{si} is the largest. In mixed-phase clouds, the partitioning of the total condensate between cloud water and cloud ice, under control of the microphysics process PBERG, is formulated as a function of temperature. The Bergeron-Findeisen process is parameterized through two different mechanisms: (1) increased amounts of cloud ice are produced at the expense of supercooled water when the temperature is low enough; and (2) enhanced conversion to precipitation is parameterized by the microphysical process PSACW. Both mechanisms act to reduce the amount of supercooled water in the cloud.

The saturation vapor pressure for temperatures between $T_{00}$and T_0, e_{sm}, is obtained by linear interpolation between the saturation vapor pressures with respect to water and ice:

$$e_{sm}(T) = \omega\, e_{sw}(T) + (1-\omega)\, e_{si}(T)\ . \tag{7}$$

Here the weight (ω) is defined as

$$\omega = \frac{T - T_{00}}{T_0 - T_{00}}, \tag{8}$$

so that $\omega = 0$ for $T = T_{00}$, and $\omega = 1$ for $T = T_0$. The saturation mixing ratio q_{sm} is computed using

$e_{sm}(T)$. The partitioning between q_c and q_i is then obtained by assuming that

$$\frac{\partial q_c}{\partial t} = \omega \frac{\partial}{\partial t}(q_c + q_i) \quad \text{and} \quad \frac{\partial q_i}{\partial t} = (1 - \omega) \frac{\partial}{\partial t}(q_c + q_i) \ . \tag{9}$$

This allows conservation of the generalized moist static energy, as explained by Fowler et al. (1995). Note that the actual partitioning between liquid and ice is not a pre-determined function of temperature.

2.3 Precipitation processes

We have chosen to explicitly time-step the precipitation process for rain and snow, using a small time step (two minutes) with a time-splitting method. This choice may seem odd, in view of the rapid fallspeeds of rain and snow particles. Considering that for a fallspeed of 5 m s^{-1}, a particle can fall through the depth of the troposphere in about 2000-3000 seconds, the assumption of instantaneous removal may seem more appropriate. Our reason for not assuming instantaneous removal, and for time-stepping the precipitation process instead, is that precipitation particles are subject to various microphysical processes as they fall. Rain and snow may evaporate, collect other particles, freeze or melt, etc. By far the simplest and most rigorous way to take these processes into account is to time-step the precipitation.

We express the tendency of rain or snow due to precipitation (P_x; in kg kg^{-1} s^{-1})[2] by

$$P_x = g \frac{d}{dp}(\rho \, q_x \, V_x) \ , \tag{10}$$

where g is the gravitational acceleration, ρ is the air density, q_x is the mixing ratio, and V_x is the fallspeed.

2.4 Interactions with cumulus convection

Stratiform clouds are coupled with convection through detrainment of cloud water and cloud ice from the tops of cumulus towers. This coupling leads to the formation of horizontally extensive upper-tropospheric anvil clouds and cirrus debris arising from deep convective activity. The parameterization of moist convection originating in the planetary boundary layer (PBL) consists of a modified version of the Arakawa-Schubert scheme (1974; see also Lord, 1982 and Lord et al., 1982). A key feature of this modified Arakawa-Schubert parameterization is that it includes a prognostic cumulus kinetic energy, as described by Randall and Pan (1993). Cumulus updrafts are assumed to originate only in the PBL and to transport mass upward in the free troposphere. The PBL mass is then replenished by turbulent entrainment and large-scale mass convergence. The partitioning of total detrained water between cloud water and cloud ice depends on temperature, following Lord (1982). For $T \geq -10^{\circ}C$, the condensate is detrained entirely as cloud water. For $T < -40^{\circ}C$, it is detrained entirely as cloud ice. In the temperature range $-40^{\circ}C \leq T < -10^{\circ}C$, the partitioning of detrained condensed water between cloud water and cloud ice depends linearly on temperature. The penetrative convec-

2. Here x refers to the subscripts r for rain, and s for snow.

tion scheme is supplemented by moist convective adjustment (Manabe et al., 1965) to remove any convective instability in the free troposphere. A dry convective adjustment scheme also mixes water vapor between adjacent layers.

In the formulation of the cumulus parameterization, it is assumed (Arakawa and Schubert, 1974) that the fractional area covered by active cumulus updrafts is negligibly small. For this reason, it is not possible, with the current cumulus parameterization, to predict the amount of water and / or ice that is stored inside the cumulus updrafts. The prognostic cloud microphysical variables of the model represent the condensed water in the stratiform clouds outside the cumulus towers, although as mentioned above the liquid water and ice detrained from the cumulus clouds do act as sources for the prognostic microphysical variables. Here we define "stratiform clouds" to be clouds which are neutrally buoyant with respect to their environment.

2.5 Interactions with radiation

The parameterization of radiative transfer at infrared and solar wavelengths follows Harshvardhan et al. (1987).

At infrared wavelengths, the upward and downward clear-sky fluxes are computed using the concept of broad band absorptivity. The radiative transfer scheme takes into account the molecular absorption-emission by H_2O following the transmission approach by Chou (1984), and also the effects of the water-vapor continuum (Roberts et al., 1976). The CO_2 absorptance model is based on the work of Chou and Peng (1983). Absorption by O_3 follows the mode of Rodgers (1968). Cloudy fluxes are obtained by computing the probability of a clear line of sight between each model layer and all other layers, the ground, and the top of the atmosphere. This probability varies depending on the choice of cloud overlap, i.e. maximum or random.

At solar wavelengths, the computation of the clear-sky fluxes follows the formulation of Lacis and Hansen (1974) for the molecular absorption by H_2O, CO_2, O_3, and Rayleigh scattering. The major difference with Lacis and Hansen (1974) is in the treatment of scattering by clouds, which is dependent upon the solar zenith angle. Assuming that the cloud optical depth, single scattering albedo, and asymmetry factor of a cloudy layer are known, cloudy fluxes are computed using the Delta-Eddington approximation (Joseph et al., 1976).

No clouds are allowed to exist in the two highest model layers located between the tropopause level (fixed at 100 mb) and the model upper boundary located at 51.3 mb. Convective and large-scale condensation clouds are considered to form in the free troposphere if the total amount of condensate exceeds 10^{-5} kg kg^{-1}. This finite threshold is necessary to hinder the formation of optically very thin high-level clouds. As the UCLA model from which it was derived, the CSU GCM does not currently include a parameterization of fractional cloudiness for stratiform clouds above the boundary layer, although we are developing one at this time (Xu and Randall, 1994; Randall, 1987). If clouds are predicted to form, their cloud fraction is set equal to 1. Clouds are assumed to be radiatively inactive otherwise. The cloud fraction of PBL clouds follow the formulation of Harshvardhan et al. (1989); their cloud fraction is set equal to 1 when they are more than 12.5 mb deep, and decreases linearly to zero as their pressure thickness decreases from 12.5 mb to zero.

The optical effects of cloud water, cloud ice, and snow are considered; those of rain are omitted. The computation of the cloud optical depth (τ^3_x) and cloud infrared emissivity (ε_x) as functions of the cloud water, cloud ice, and snow path (W_x; with dimensions of mass per unit area) follows the formulation of Stephens (1978) and Harshvardhan et al. (1989), respectively:

$$\tau_x = \frac{3}{2}\frac{W_x}{r_e} \tag{11}$$

and

$$\varepsilon_x = 1 - \exp(-\kappa\tau_x) \ . \tag{12}$$

The effective radius (r_e) is set equal to 10 μm for cloud water, 30 μm for cloud ice, and 1000 μm for snow, respectively. Here κ is the infrared absorption coefficient and is set equal to 0.75 m^2g^{-1}. The single scattering albedo of cloud water (ω_{0c}) is set equal to 0.99 while those of cloud ice (ω_{0i}) and snow (ω_{0s}) are both set equal to 0.98. The asymmetry factors for cloud water (g_c), cloud ice (g_i), and snow (g_s) are assumed to be 0.85, 0.75, and 0.75, respectively. The optical depth and infrared emissivity of mixed-phase clouds are computed following Rockel et al. (1991).

3. MOISTURE AND RADIATIVE BUDGET

Briefly, the core of the CSU GCM is based on a version of the UCLA GCM, as described by Harshvardhan et al. (1989), and Randall et al. (1989). The version used here is a 17-level grid-point model with a horizontal resolution of 4° in latitude by 5° in longitude. The vertical discretization is based on a modified σ-coordinate in which the planetary boundary layer is the bottom layer of the model (Suarez et al., 1983). Results presented here were obtained from a full annual cycle simulation, after a three-month spin-up. The initial atmospheric states for both runs correspond to October 1st of a prior long-term climate simulation performed without cloud microphysics. The initial mixing ratios of cloud water, cloud ice, rain, and snow were set to zero. Sea-surface temperatures follow seasonally varying climatology. Full solar and infrared radiative transfer calculations were made every hour to take into account the diurnal variations of radiation and clouds. At present, convection is computed every hour. The dynamics time-step is 6 minutes. The cloud microphysics scheme is embedded in the model dynamics and uses a 2 minute time-step, so that precipitation of rain and snow can be computed explicitly.

3.1 Atmospheric moisture budget

Figure 2 shows January maps of the vertically integrated amounts of cloud water (CW), cloud ice (CI), rain (RW), and snow (RI). Figure 3 presents latitude-height cross sections of the zonally averaged CW, CI, RW, and RI, also for January.

---

3. x refers to the subscripts c for cloud water, i for cloud ice, and s for snow.

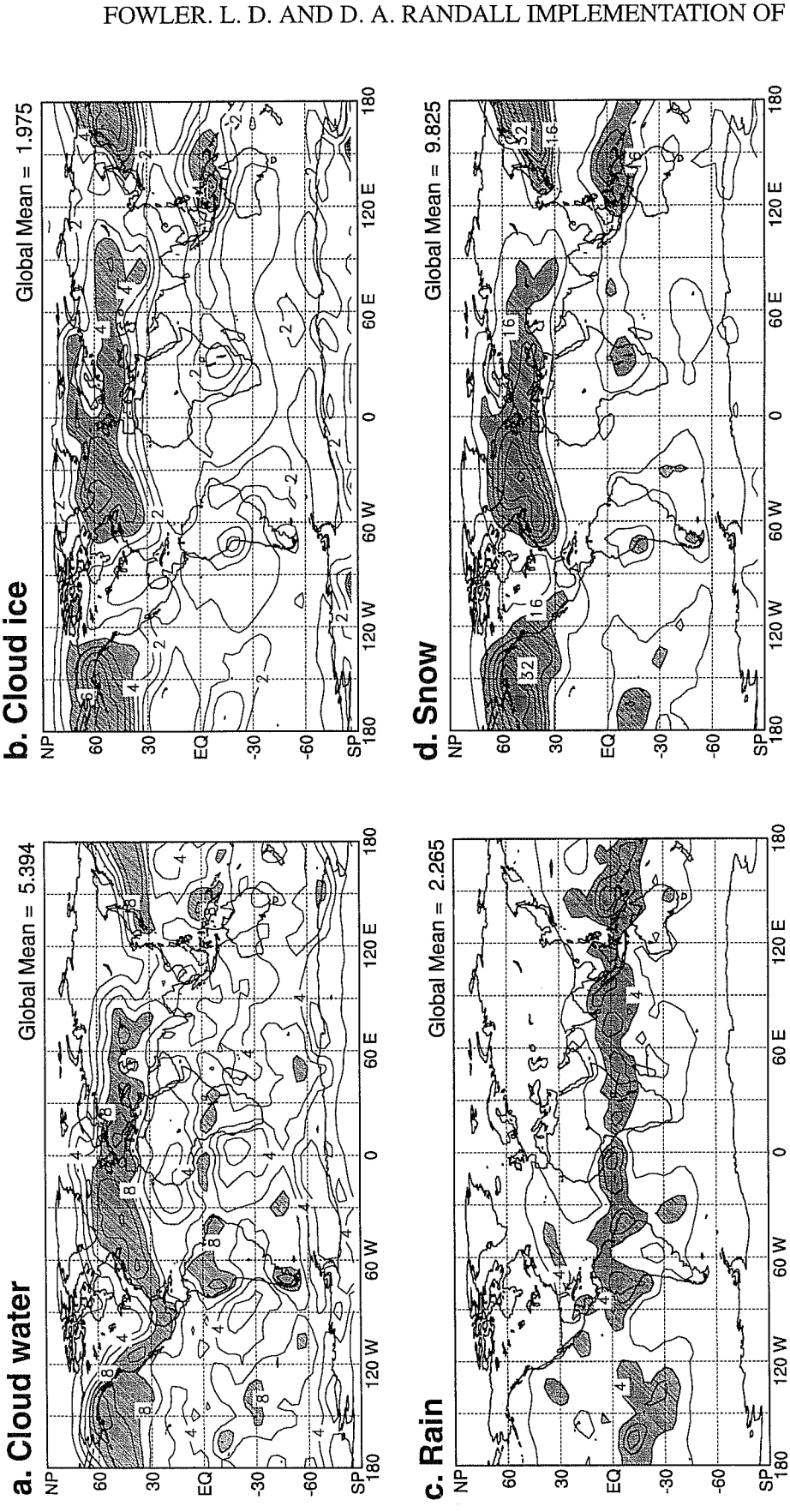

Fig. 2. Maps of the monthly averaged vertically integrated (a) cloud water, (b) cloud ice, (c) rain, and (d) snow, for January. In (a), contour intervals are every $2x10^{-2}$ kg m^{-2}, and heavy shading corresponds to values greater than $8x10^{-2}$ kg m^{-2}. In (b), contour intervals are every $1x10^{-2}$ kg m^{-2}, and heavy shading corresponds to values greater than $4x10^{-2}$ kg m^{-2}. In (c), contour intervals are every $2x10^{-2}$ kg m^{-2}, and heavy shading corresponds to values greater than $4x10^{-2}$ kg m^{-2}. In (d), contour intervals are every $8x10^{-2}$ kg m^{-2}, and heavy shading corresponds to values greater than $16x10^{-2}$ kg m^{-2}.

Cloud water and cloud ice are detrained at the tops of cumulus towers, primarily over the deep tropical regions of convective activity. They are also produced by large-scale supersaturation, primarily in the tropics and the middle latitudes. As may be seen in Fig. 2, maxima of CW and CI are located over the chief tropical convective activity regions in conjunction with strong detrainment of condensed water, and over the North Pacific and North Atlantic storm track regions in January in conjunction with midlatitude cyclone activity. CW and CI are more abundant in the cool middle latitudes than in the warm tropics. On a global average for January, CW is equal to 0.054 kg m^{-2}, whereas CI is equal to 0.020 kg m^{-2}.

The vertical distributions of CW and CI are naturally quite different. CW displays two primary maxima in the lower troposphere in the middle latitudes, and a secondary maximum in the tropics, located near the 8 km level. This suggests that cloud water results predominantly from large-scale supersaturation. In contrast, CI shows a primary maximum in the tropical upper troposphere, and a secondary maximum in the middle latitudes in the winter hemisphere. In the tropics, the primary maximum of CI is higher than and stronger than the secondary maximum of CW. This indicates that CI results predominantly from the detrainment of cloud ice at the tops of cumulus towers.

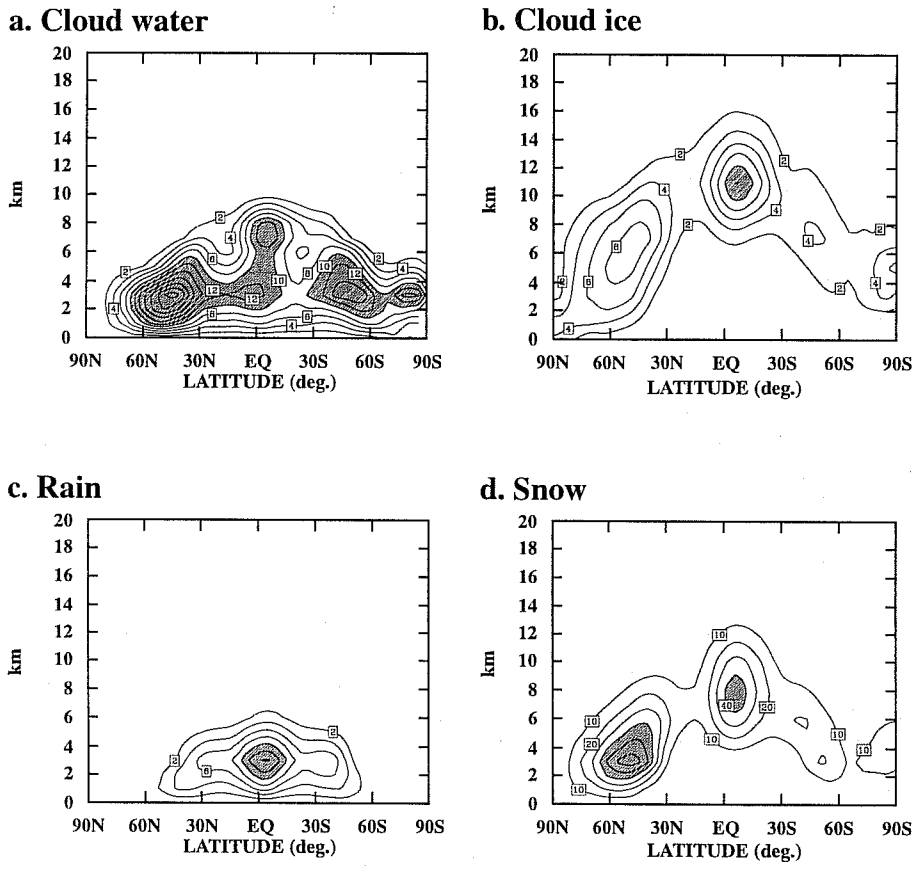

Fig. 3. Latitude-height cross sections of (a) the cloud water, (b) the cloud ice mixing, (c) the rain, and (d) the snow mixing ratio. In (a), (b), and (c), contour intervals are every $2x10^{-6}$ kg kg^{-1}, and heavy shading corresponds to values greater than $10x10^{-6}$ kg kg^{-1}. In (d), contour intervals are every $10x10^{-6}$ kg kg^{-1}, and heavy shading corresponds to values greater than $40x10^{-6}$ kg kg^{-1}.

Because rain and snow are produced by autoconversion and collection of cloud water and cloud ice, there is a strong correspondence between the distributions of CW and RW, and CI and RI. In January, RW is largest over the tropical convective activity centers, and results from autoconversion and collection of cloud water by rain, plus melting of snow falling in from aloft. The contribution of melting snow to RW is quite significant and results from the strong removal of cloud ice from the upper troposphere by autoconversion of cloud ice to snow. In contrast, RI is largest at high latitudes, and results from autoconversion and collection of cloud ice by snow (enhanced by the Bergeron-Findeisen process), and much less importantly from freezing of rain. The latitude-height distribution of RI is similar to that of CI, except that the maxima of RI are of course located below those of CI.

3.2 Comparison between simulated and satellite derived CW

We compare the simulated CW against columnar cloud water data retrieved from SSM/I observations over the oceans (Greenwald et al., 1993). Figure 4 shows the monthly mean global distribution of the vertically integrated CW retrieved from SSM/I measurements for January, as well as the zonally averaged profiles of the simulated and satellite-derived CW.

Although the model qualitatively reproduces the main geographical features seen in the satellite data, there are quantitative differences between the simulation and the observations. One major discrepancy is that the model underpredicts CW along the ITCZ, as very clearly seen when comparing Fig. 4.a with 2.a, and comparing the zonally averaged distributions of the simulated and observed CW in Fig. 4.b. In the observations, the ITCZ is very well delineated as a narrow band of high cloud water amounts across the Pacific and Atlantic Oceans. Although the simulated ITCZ is also clearly marked across both oceans, its intensity is not as strong as that seen in the observations. The model underestimates CW in the middle latitudes in the summer hemisphere. In particular, comparison of the January maps between Figs. 4.a and 2.a shows that the model strongly underestimates CW over the Southern Oceans. There is reasonable agreement between the simulated and observed CW for the storm track regions in the winter hemisphere, although the simulated peak in CW is not as broad as that in the observations.

Before drawing any definitive conclusions on the ability of the cloud microphysics scheme to predict the actual cloud water amount, we need to keep in mind that the retrieval of cloud water from microwave measurements is far from trivial, even over the oceans. Greenwald et al. (1993) caution that satellite-derived cloud water estimates have a theoretical relative error typically ranging between 25% and 40%, depending on the atmospheric and surface conditions, and the amount of liquid water present in the cloud. Also, retrievals are known to be less accurate in precipitating than non-precipitating cloud systems due to contamination by rain drops. SSM/I does not "see" large, precipitating drops; in effect it senses only drops smaller than some threshold radius. Similarly, the "cloud water" variable of EAULIQ does not include large, precipitating drops; it represents only the liquid water mass associated with drops smaller than some threshold radius. A problem, however, is that these two threshold radii are not necessarily the same, and we are unable, at this stage, to clearly define the relationship between them. This problem complicates the interpretation of discrepancies between the simulated and SSM/I-observed cloud water distributions.

In addition, we should remember that the simulated CW values reported here do not include the CW in PBL clouds. We thus expect the simulated values to be less than the observed.

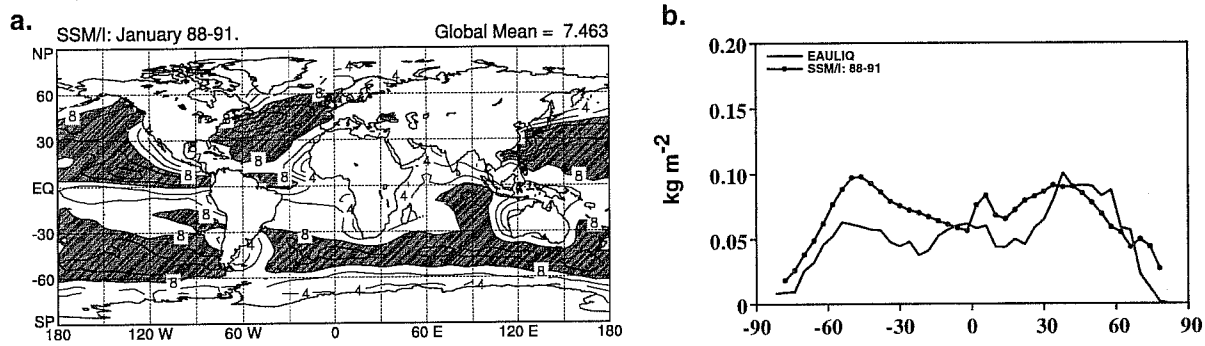

Fig. 4. (a) Map of the monthly averaged vertically integrated cloud water retrieved from SSM/I satellite data, for January. Contour intervals are every $2x10^{-2}$ kg m^{-2}, and heavy shading corresponds to values greater than $8x10^{-2}$ kg m^{-2}; (b) zonally averaged distributions of the monthly averaged vertically integrated cloud water simulated by the CSU GCM, and retrieved from SSM/I data, for January.

3.3 Cloud radiative forcing

Figure 5 compares January maps of the longwave (CFL) and shortwave (CFS) cloud radiative forcings simulated by the CSU GCM against ERBE derived satellite observations. In Fig. 5, CFL and CFS were computed using Method 2 of Cess and Potter (1987). The geographical distributions of the simulated and satellite-derived radiation fields appear to be in very reasonable agreement, at both long and short wavelengths. However, the model has the tendency to overestimate CFL over the areas of strong CFL, as above the deep tropical convective activity regions and the Northern Hemisphere storm track regions. Also, the extent of areas of weak CFL, as above the subtropical oceans and the desert regions over the continents, are underestimated by the model. The simulated CFS is overestimated over the deep tropical convective activity regions and the Southern Oceans when compared against satellite data. The globally averaged simulated CFL is equal to 32.7 W m^{-2} versus 28.7 W m^{-2} from ERBE data. At short wave lengths, the globally averaged CFS is equal to -59.2 W m^{-2}, versus -53 W m^{-2} as derived from satellite observations. A more complete comparison between the simulated planetary radiation budget and ERBE satellite data may be found in Fowler and Randall (1995a).

4. SENSITIVITY TO MODELING ASSUMPTIONS

We have investigated the sensitivity of the climate simulated with the CSU GCM to various aspects of the parameterization of the cloud microphysical processes and its interactions with the cumulus convection and radiative transfer parameterizations (Fowler and Randall, 1995b). Several 120-day sensitivity experiments corresponding to perpetual January conditions were performed. They were compared to a control simulation

a. Longwave cloud radiative forcing

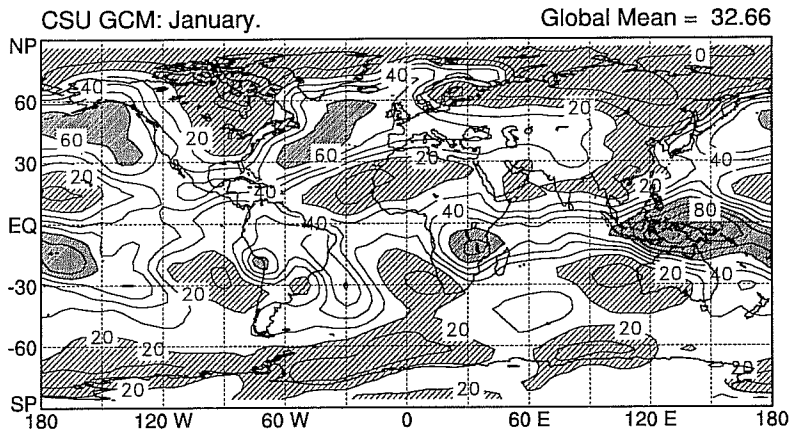

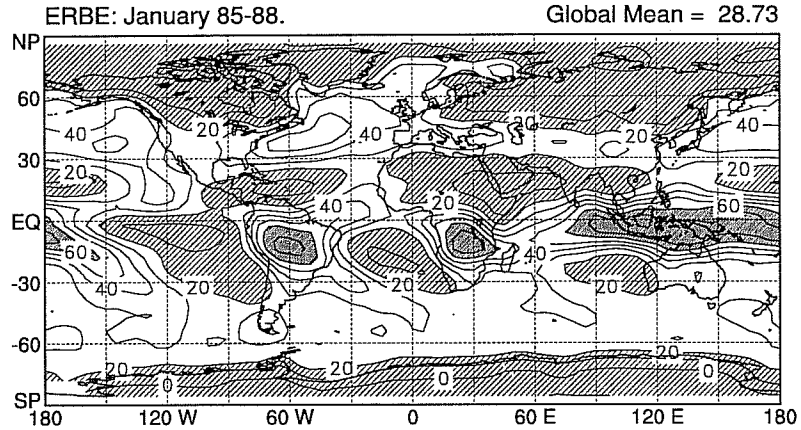

b. Shortwave cloud radiative forcing

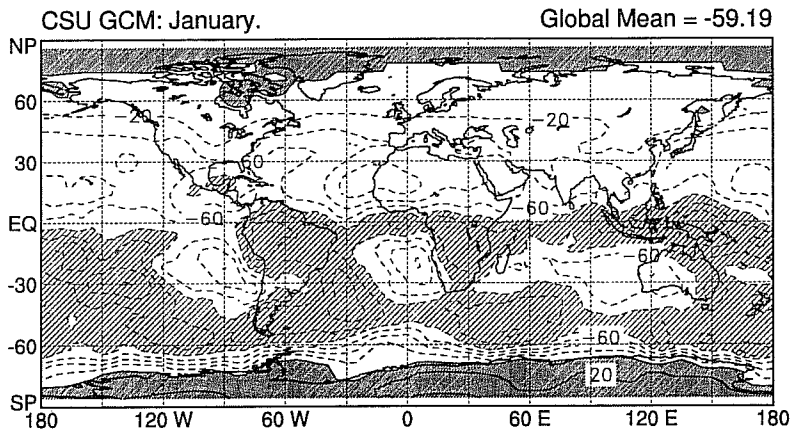

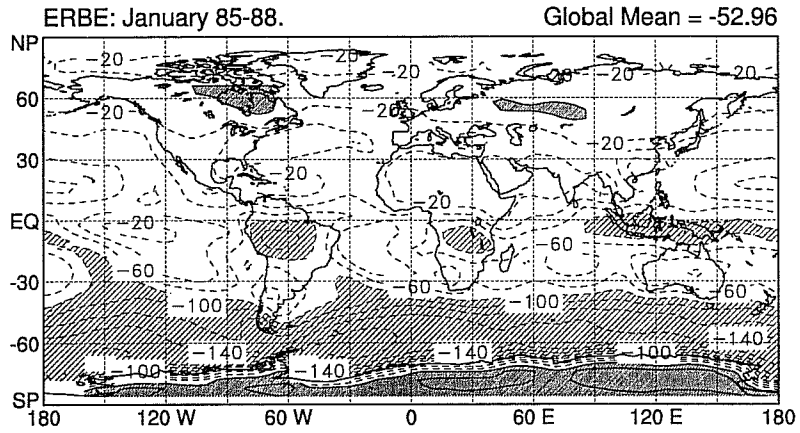

Fig. 5. Maps of the monthly averaged (a) longwave cloud radiative forcing, and (b) shortwave cloud radiative forcing simulated by the CSU GCM, and derived from ERBE data, for January. In (a), contour intervals are every 10 W m^{-2}. Light shading corresponds to values less than 20 W m^{-2}, and heavy shading corresponds to values greater than 60 W m^{-2}. In (b), contour intervals are every 20 W m^{-2}. Light shading corresponds to values less than -100 W m^{-2}, and heavy shading corresponds to values greater than 0 W m^{-2}.

(hereafter referred to as ELQJAN) using the same version of the model as Section 3, but with fixed top-of-the atmosphere insolation and surface boundary conditions. Here, we report the sensitivity of the CSU GCM to our parameterization of the Bergeron-Findeisen mechanism, and the thresholds of autoconversion of cloud water to rain and cloud ice to snow.

4.1 Impact of mixed-phase clouds

In this section, we analyze the differences in the climate simulated by the CSU CGM when mixed-phase clouds are allowed to form in the temperature range $-20^{o}C \leq T < 0^{o}C$ (ELQJAN), $-40^{o}C \leq T < 0^{o}C$ (BERG40), or when no mixed-phase clouds are allowed to form (NOBERG). We define mixed-phase clouds as clouds that form at grid-points where supercooled cloud water and cloud ice coexist, i.e. where the Bergeron-Findeisen process (PBERG) is active. Parameterization of PBERG is described in Fowler et al. (1995; refer to Section 2.b, and Appendix A). In ELQJAN, cloud ice and supercooled cloud water are allowed to coexist in the temperature range $-20^{o}C \leq T < 0^{0}C$. At temperatures colder than -20°C, supercooled cloud water is assumed to freeze instantaneously as cloud water. At temperatures warmer than 0°C, cloud ice is assumed to melt instantaneously as cloud water. As the temperature range over which PBERG is allowed to occur widens, the amount of supercooled cloud water increases at the expense of cloud ice. The amount of mixed-phase clouds strongly influences the top-of-the atmosphere longwave and shortwave radiation budgets since the cloud optical properties depend on the partitioning between cloud water and cloud ice. The infrared emissivity (ε), optical depth (τ), single scattering albedo (ω_0) and asymmetry factor (g) of mixed-phase clouds are computed using Eqs. (2), (3), (4), and (5) of Fowler and Randall (1995a). In ELQJAN, BERG40, and NOBERG, the cloud optical properties of PBL clouds follow the formulation of Harshvardhan et al. (1989) which is also described in Fowler and Randall (1995a), since the cloud microphysics parameterization is not applied to the PBL.

Figure 6 shows the latitude-height cross sections of the zonally averaged differences between CW and CI simulated by BERG40 and ELQJAN, and NOBERG and ELQJAN. In BERG40, supercooled cloud water increases at the expense of cloud ice between the isotherms -40°C and -20°C. In NOBERG, the reverse happens and cloud ice increases at the expense of supercooled cloud water. It is interesting to note that, in BERG40, the increase in CW (on a global average, + 0.008 kg m^{-2}) does not exactly compensate the decrease in CI (-0.003 kg m^{-2}). This results from our assumption that supercooled cloud water may be converted to snow with the same autoconversion threshold as that used to convert cloud water to rain (q_{c0} = 0.1 kg kg^{-1}). In contrast, the autoconversion threshold for cloud ice to snow is 0.01 kg kg^{-1} which forces cloud ice to be removed from the atmosphere faster than supercooled cloud water. A closer compensation is observed in NOBERG, for which the decrease in CW is -0.006 kg m^{-2} while the increase in CI is +0.004 kg m^{-2}.

Results indicate that the sum CW+CI+RI which determines the occurrence of clouds and their cloud optical properties, varies very little among the three experiments. CW+CI+RI is equal to 0.143 kg m^{-2} in ELQJAN, versus 0.154 kg m^{-2} in BERG40, and 0.110 kg m^{-2} in NOBERG. In turn, this change in CW+CI+RI yields a change in the globally-averaged cloud fraction of +1.7% between BERG40 and ELQJAN, and of -2.8% be-

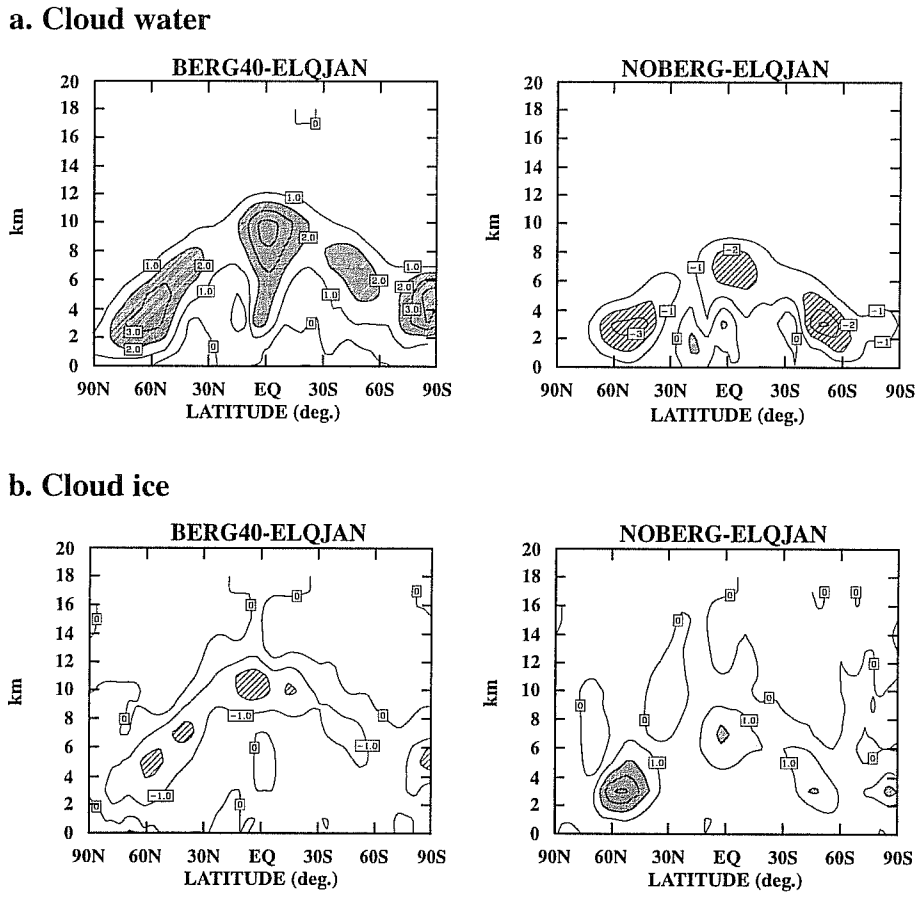

Fig. 6. Latitude-height cross sections of the zonally averaged differences in (a) the cloud water mixing ratio, and (b) the cloud ice mixing ratio, between BERG40 and ELQJAN, and NOBERG and ELQJAN. Contour intervals are every $1x10^{-6}$ kg kg^{-1}. Light shading corresponds to values less than $-1x10^{-6}$ kg kg^{-1}. Heavy shading corresponds to values greater than $2x10^{-6}$ kg kg^{-1}.

tween NOBERG and ELQJAN. Hence, the change in the cloud optical depth and cloud infrared emissivity among the three experiments essentially results from the change in the partitioning between the amounts of cloud water and cloud ice.

Figure 7 shows the latitude-height cross sections of the zonally averaged differences between the cloud optical depth and effective cloud cover[4] simulated by BERG40 and ELQJAN, and NOBERG and ELQJAN. The effective cloud fraction is defined as the cloud fraction times the cloud infrared emissivity. In BERG40, the increased supercooled cloud water leads to an increased cloud optical depth and effective cloud cover for middle- and high-level clouds. The reasons are that: 1) the cloud optical depth is proportional to the cloud water path which is greater in BERG40 than in ELQJAN, and 2) the cloud optical depth is inversely proportional to the effective radius which is smaller for cloud water (10 μm) than for cloud ice (30 μm). Referring to Eq. (12), we see that larger cloud optical depths yield larger cloud infrared emissivities and hence greater effective cloud cover, providing that the cloud fraction remains constant. The results of NOBERG show a decrease

4. The effective cloud cover is defined as the cloud fraction times the cloud infrared emissivity.

of the cloud optical depth and effective cloud cover for middle- and high-level clouds in the tropics and the middle latitudes. This decrease results because the increase in cloud ice does not exactly compensate the decrease in cloud water, and the effective radius for cloud ice is less than that for cloud water.

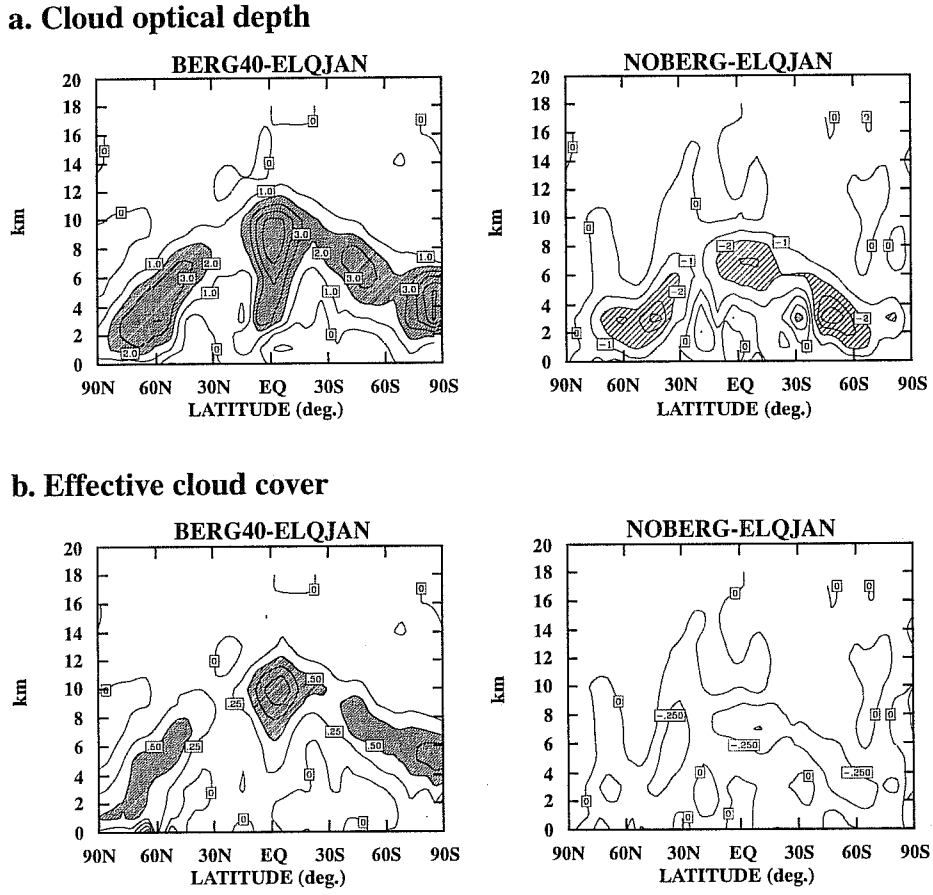

Fig. 7. Latitude-height cross sections of the zonally averaged differences in (a) the cloud optical depth, and (b) the effective cloud cover, between BERG40 and ELQJAN, and NOBERG and ELQJAN. In (a), contour intervals are every $1x10^{-3}$ mb^{-1}. Light shading corresponds to values less than $-2x10^{-3}$ mb^{-1}. Heavy shading corresponds to values greater than $2x10^{-3}$ mb^{-1}. In (b), contour intervals are every $0.25x10^{-3}$ mb^{-1}. Light shading corresponds to values less than $-5x10^{-3}$ mb^{-1}. Heavy shading corresponds to values greater than $0.5x10^{-3}$ mb^{-1}.

Finally, Fig. 8 shows the distributions of the zonally averaged longwave and shortwave cloud radiative forcings obtained with in three experiments. When compared to ELQJAN, BERG40 leads to increased long and short wave cloud radiative forcing whereas NOBERG leads to decreased forcing at all latitudes. These variations are in accordance with the change in the cloud optical properties described above. Optically thicker (thinner) clouds increase (decrease) the amount of shortwave solar radiation reflected at cloud tops, hence enhancing the radiative effect of clouds at short wave lengths. Also, increasing (decreasing) the effective cloud fraction yields a decreased (increased) outgoing infrared radiation, hence enhancing (decreasing) the long wave cloud radiative forcing. On a global average and relative to ELQJAN, the radiative effects of clouds changes by +4.1 W m^{-2} in BERG40 and -2.0 W m^{-2} in NOBERG at infrared wave lengths, and by -5.8 W m^{-2} in BERG40 and +4.4 W m-2 in NOBERG at solar wave lengths.

It is interesting to note that although we change the width of the temperature window over which PBERG is active by the same increment (we increased it by 20°C in BERG40 and decreased it by 20°C in NOBERG), the model response is stronger in BERG40 than in NOBERG. For instance, the increase in supercooled cloud water in BERG40 is greater than the increase in cloud ice in NOBERG. The absolute change in the cloud radiative forcing between BERG40 and ELQJAN is greater than between NOBERG and ELQJAN. The difference in the strength of the model response between the two experiments is due to the fact that the microphysics and the optical properties of water clouds and ice clouds are parameterized differently. The thresholds for autoconversion of supercooled cloud water and cloud ice to snow are different, hence allowing supercooled cloud water to remain suspended in the atmosphere longer than cloud ice. The effective radius for cloud water is smaller than that for cloud ice, hence leading to cloud optical depths and infrared emissivities that are greater in BERG40 than in NOBERG.

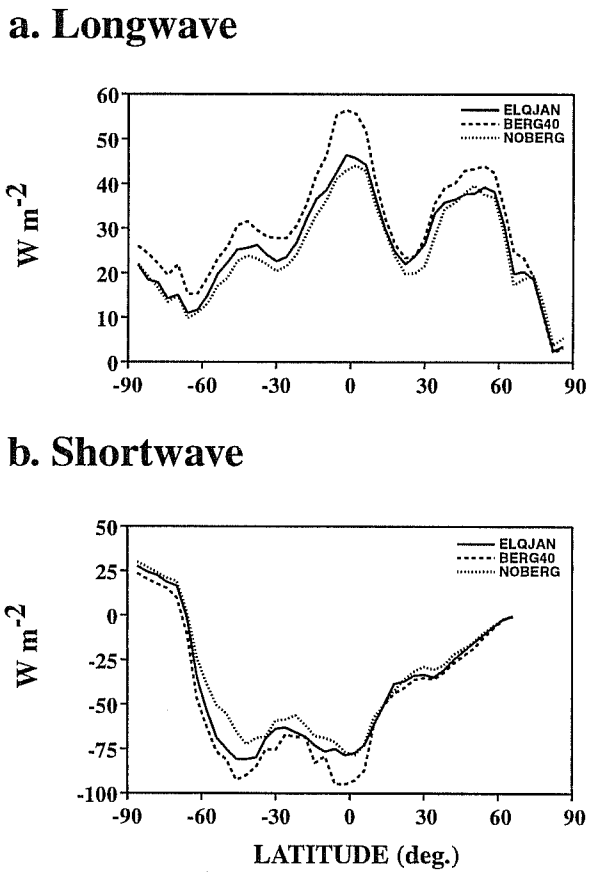

Fig. 8. Zonally averaged of (a) the longwave cloud radiative forcing, and (b) the shortwave cloud radiative forcing, simulated by ELQJAN, BERG40, and NOBERG.

4.2 Impact of autoconversion thresholds

Two of the most important parameters of our cloud microphysics parameterization are the thresholds for autoconversion of cloud water to rain (q_{c0}) and cloud ice to snow (q_{i0}). q_{c0} and q_{i0} are prescribed values above which cloud water and cloud ice are converted to rain and snow until their mixing ratios do not exceed q_{c0}

and q_{i0}. In Fowler et al. (1994) and Fowler and Randall (1995a), q_{c0} and q_{i0} were adjusted so that the simulated vertically integrated cloud water was in reasonable agreement with cloud water estimates derived from SSM/I microwave radiances, and the geographical distributions of the simulated outgoing infrared radiation and planetary albedo resembled those obtained from ERBE data. Note that only these two numerical constants were adjusted in this way.

The appropriate values of q_{c0} and q_{i0} are strongly dependent upon the spatial resolution of the GCM, and on the parameterization of the fractional cloudiness. Our particular choices for q_{c0} and q_{i0} arise from the coarse horizontal resolution of our model, and from our current lack of fractional cloudiness parameterization. As mentioned earlier, each model grid-box is assumed to be either overcast or cloud-free. Any condensed water is assumed to be uniformly distributed over the whole grid-box, and so autoconversion thresholds have to be drastically reduced to hinder the formation of excessively widespread and thick cloud water and cloud ice shields.

In QCW0 and QCI0, the impacts of increasing q_{c0} and q_{i0} are discussed separately. In QCW0, q_{c0} is increased from 0.1 g kg^{-1} to 0.3 g kg^{-1} while, in QCI0, q_{i0} is increased from 0.01 g kg^{-1} to 0.03 g kg^{-1}. In contrast, q_{c0} is set equal to 0.7 g kg^{-1} in Rutledge and Hobbs (1983; 1984) while q_{i0} is equal to 0.1 g kg^{-1} in Lin et al. (1983).

Figure 9 shows the zonally averaged distributions of the vertically integrated cloud water simulated by ELQJAN and QCW0, and cloud ice mixing ratios simulated by ELQJAN and QCI0. The increase in CW between QCW0 and ELQJAN is shown to be almost uniform between 60°N and 60°S while, in contrast, the increase in QCI between QCI0 and ELQJAN is the strongest in the middle latitudes in the winter hemisphere. On a global average, CW jumps from 0.03 kg m^{-2} in ELQJAN to 0.07 kg m^{-2} in QCW0. CI increases from 0.02 kg m^{-2} in ELQJAN to 0.03 kg m^{-2} in QCI0.

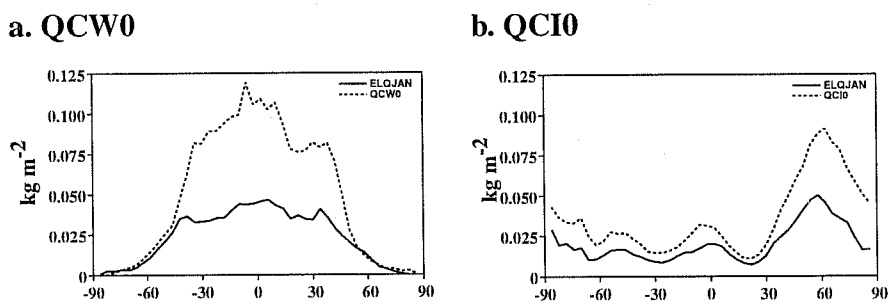

Fig. 9. Zonally averaged distributions of the vertically integrated (a) cloud water mixing ratio simulated by ELQJAN and QCW0, and (b) cloud ice mixing ratio simulated by ELQJAN and QCI0. Units are in kg m^{-2}.

Figure 10 shows the latitude-height cross sections of the differences in the zonally averaged cloud optical depth and effective cloud cover between QCW0 and ELQJAN, and between QCI0 and ELQJAN. As expected, the increase in CW between QCW0 and ELQJAN yields a significant increase in the cloud optical depth

of low- and middle-level clouds below 6 km between 60°N and 60°S, i.e. clouds which mean temperature is greater than -20°C. In contrast, the increase in the cloud optical depth of ice clouds between QCI0 and ELQJAN is small, even at 60°N where Fig. 9 showed the largest increase in CI. The difference in the increase of the cloud optical depth between water and mixed-phase clouds, and ice clouds results because the optical depth is inversely proportional to the effective radius which is set equal to 10 μm for cloud water, and 30 μm for cloud ice, respectively.

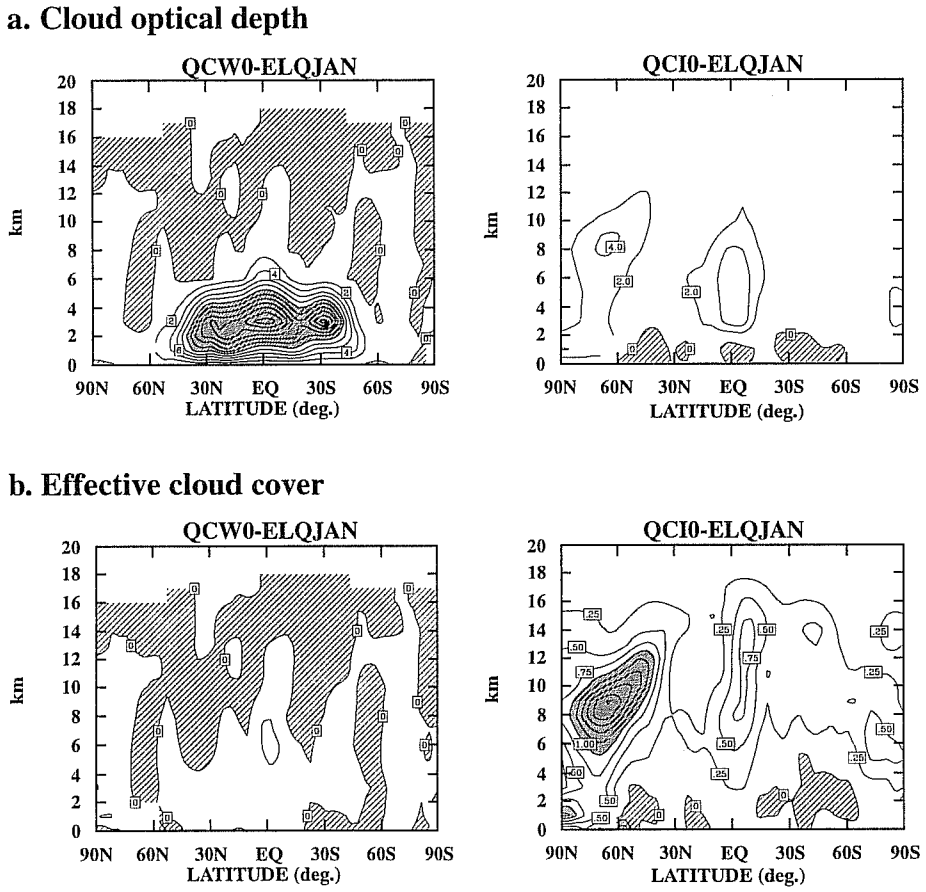

Fig. 10. Latitude-height cross sections of the differences in (a) the cloud optical depth, and (b) the effective cloud cover between QCW0 and ELQJAN, and between QCI0 and ELQJAN. In (a), contour intervals are every $2x10^{-3}$ mb^{-1}. Light shading corresponds to values less than $0x10^{-3}$ mb^{-1}. Heavy shading corresponds to values greater than $10x10^{-3}$ mb^{-1}. In (b), contour intervals are every $0.25x10^{-3}$ mb^{-1}. Light shading corresponds to values less than 0. Heavy shading corresponds to values greater than $1x10^{-3}$ mb^{-1}.

As shown in Fig. 10, the increase in CW between QCW0 and ELQJAN yields very little difference in the vertical distribution of the effective cloud cover. In contrast, the increase in CI between QCI0 and ELQJAN produces a significant increase in the effective cloud cover of upper-tropospheric clouds in the tropics and in the middle latitudes in the Northern Hemisphere. There are two reasons for this. First, QCW0 leads to small increases in the fraction of low- and middle-level clouds whereas QCI0 leads to a large increase in the fraction of high-level clouds. On a global average, low- and middle-level clouds increase by +5% and +1.6% in QCW0, respectively. In contrast, the fraction of high-level clouds increases by +9.8% in QCI0. Second, the re-

lationship between the cloud optical depth and the infrared emissivity given by Eq. (12) indicates that, for optically thick water clouds, a large increase in the cloud optical depth will not significantly alter the cloud infrared emissivity, which is already close to 1. In contrast, a small increase in the cloud optical depth of optically thin ice clouds will lead to a rapid increase in the cloud infrared emissivity.

Finally, we looked at the change in the total precipition rate between ELQJAN, QCW0, and QCI0. Figure 11 shows the zonally averaged distribution of the precipitation rates simulated by the three experiments. The precipitation rate simulated by QCW0 is very much the same as that simulated by ELQJAN. In contrast, that simulated by QCI0 is systematically less than that simulated by ELQJAN, especially along the equator, and in the middle latitudes in the Northern Hemisphere. As explained in Fowler and Randall (1994), the decrease in the precipitation rates between QCI0 and ELQJAN results because of the decrease in the atmospheric radiative cooling, and increased static stability of the atmosphere between the two experiments, in response to an increase of high-level cloudiness in QCI0.

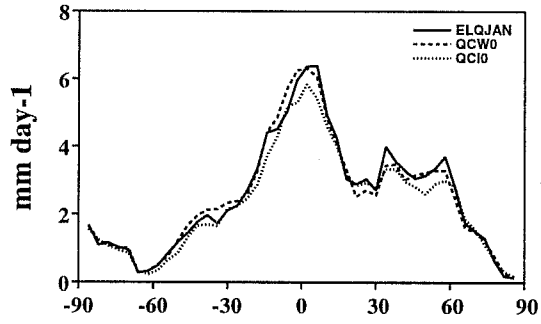

Fig. 11. Zonally averaged distribution of the total precipitation rate simulated by ELQJAN, QCW0, and QCI0, for January.

5. SUMMARY

We have briefly described the design of a bulk cloud microphysics parameterization that has been designed to simulate stratiform cloudiness. Our objectives were to introduce a physically based representation of the sources and sinks of the main components of the atmospheric moisture budget, and to couple the hydrological cycle and radiation through interactive cloud optical properties. The temporal and spatial evolutions of water vapor, cloud water, cloud ice, rain, and snow are determined by various cloud microphysics processes and advective processes. The microphysics of water clouds, mixed-phase clouds, and ice clouds are treated separately. Details of the cloud microphysics parameterization include a continuous collection equation to simulate collection of cloud water and cloud ice by rain and snow, as well as the Bergeron-Findeisen mechanism. An additional feature of the cloud model is the coupling between stratiform clouds and convection through the detrainment of cloud water and cloud ice.

Results of an annual-cycle simulation were discussed for the months of January. The cloud microphysics parameterization produces realistic geographical distributions of the vertically integrated cloud water, cloud ice, rain, and snow. Sources of simulated cloud water and cloud ice are located where they should be expected, i.e. in the tropical convective activity centers over land and oceans, and in the mid-latitude storm tracks. In the model, the chief source of cloud water is low-level large-scale supersaturation, whereas detrainment at the tops of cumulus towers is most important for cloud ice, especially in the tropics. Also, the vertical distribution of cloud ice highlights the importance of deep convection for upper-tropospheric stratiform clouds. Maps of the simulated longwave and shortwave cloud radiative forcings show good agreement between the simulated radiative fields and ERBE satellite data.

In including a bulk cloud microphysics parameterization developed for mesoscale models into a GCM, one is forced to 1) limit the number of water species and the number of cloud microphysics processes that may be included; and 2) deal with the tuning of a large possible number of cloud microphysics parameters that are suitable for mesoscale models and, a priori, not for large-scale models. For instance, and in contrast to standard cloud microphysics parameterizations in mesoscale models, hail and graupel were neglected, and melting and freezing processes were assumed to be instantaneous. Our cloud microphysics parameterization does not include a prognostic equation for the number concentration of cloud water droplets and cloud ice crystals at this time. The details of ice nucleation were omitted and we choose, instead, to represent condensation/evaporation and deposition/sublimation processes in a simplified manner, by using identical relaxation times.

The most difficult task in evaluating our cloud microphysics scheme is the comparison of our results with observations. Only the global distribution of columnar water vapor and cloud water over the oceans can be compared against estimates from satellites. No corresponding data are available for cloud ice, rain, or snow. Although the global oceanic observations of cloud water are extremely valuable, uncertainties inherent to the numerous difficulties in retrieving cloud water data from passive microwave radiation measurements make them far from completely reliable. In addition, global observations of cloud ice are sorely needed.

6. ACKNOWLEDGEMENTS

This research was sponsored by the National Science Foundation under grant ATM-8907414, by NASA under grant NAG-1-1266, and by the ARM program of the U. S. Department of Energy under grant DE-FG02-92ER61363, all to Colorado State University. Computing resources were provided by the Scientific Computing Division at the National Center for Atmospheric Research, by the National Center for Computational Sciences at NASA/Goddard, and by the National Energy Research Computer Center at Lawrence Livermore National Laboratory.

Our thanks to Cindy Carrick for editing this manuscript. We are grateful to ECMWF to invite us to this workshop.

7. REFERENCES

Arakawa, A., 1975: Modelling clouds and cloud processes for use in climate models. In: GARP Publication Series No. 16, ICSU/WMO, pp. 183-197.

Arakawa, A., and W.H. Schubert, 1974: The interactions of a cumulus cloud ensemble with the large-scale environment, Part I. J. Atmos. Sci., 31, 674-701.

Bergeron, T., 1935: In: On the physics of clouds and precipitation. Proc. 5th Assembly UGGI Lisbon, 2.

Chou, M.D., 1984: Broad band water vapor transmission functions for atmospheric IR flux computations. J. Atmos. Sci., 41, 1775-1778.

Chou, M.D., and L. Peng, 1984: A parameterization of the absorption in the 15 μm CO_2 spectral region with application to climate sensitivity studies. J. Atmos. Sci., 32, 409-418.

Fowler, L.D., and D.A. Randall, 1994: A global radiative-convective feedback. Geophys. Res. Let., 21, 2035-2038.

Fowler, L.D., D.A. Randall, and S.A. Rutledge, 1995: Liquid and ice cloud microphysics in the CSU General Circulation Model: Part I. Model description and simulated microphysical processes. (Submitted to J. Clim.)

Fowler, L.D., and D.A. Randall, 1995a: Liquid and ice cloud microphysics in the CSU General Circulation Model: Part II. Impact on cloudiness, the Earth's Radiation Budget, and the General Circulation of the Atmosphere. (Submitted to J. Clim.)

Fowler, L.D., and D.A. Randall, 1995b: Liquid and ice cloud microphysics in the CSU General Circulation Model: Part III. Sensitivity to modeling assumptions. (Submitted to J. Clim.)

Greenwald, T.J., G.L. Stephens, T.H. Vonder Haar, and D.L. Jackson, 1993: A physical retrieval of cloud liquid water over the global oceans using Special Sensor Microwave/Imager (SSM/I) observations. J. Geophys. Res., 98, 18,471-18,448.

Harshvardhan, R. Davies, D.A. Randall, and T.G. Corsetti, 1987: A fast radiation parametrization for atmospheric general circulation models. J. Geophys. Res., 92, 1009-1016.

Harshvardhan, D.A. Randall, T.G. Corsetti, and D.A. Dazlich, 1989: Earth radiation budget and cloudiness simulations with a general circulation model. J. Atmos. Sci., 46, 1922-1942.

Joseph, J.H., W.J. Wiscombe, and J.A. Weinman, 1976: The Delta-Eddington approximation for radiative flux transfer. J. Atmos. Sci., 33, 2452-2459.

Lacis, A.A., and J.E. Hansen, 1974: A parameterization for the absorption of solar radiation in the Earth's atmosphere. J. Atmos. Sci., 31, 118-133.

Lin, Y.-L., R.D. Farley, and H.D. Orville, 1983: Bulk parameterization of the snow field in a cloud model. J. Clim. Appl. Meteor., 22, 1065-1092.

Lord, S.J., 1982: Interaction of a cumulus cloud ensemble with the large-scale environment. Part III: Semiprognostic test of the Arakawa-Schubert cumulus parameterization. J. Atmos. Sci., 39, 88-103.

Lord, S.J., W.C. Chao, and A. Arakawa, 1982: Interaction of a cumulus ensemble model with the large-scale environment. Part IV: The discrete model. J. Atmos. Sci., 39, 104-113.

Manabe, S., J. Smagorinsky, and R.F. Strickler, 1965: Simulated climatology of a general circulation model with a hydrological cycle. Mon. Wea. Rev., 93, 769-798.

Randall, D.A, 1987: Turbulent fluxes of liquid water and buoyancy in partly cloudy layers. J. Atmos. Sci., 44, 850-858.

Randall, D.A., Harshvardhan, D.A. Dazlich, and T.G. Corsetti, 1989: Interactions among radiation, convection, and large-scale dynamics in a general circulation model. J. Atmos. Sci., 46, 1943-1970.

Randall, D.A., and D.-M. Pan, 1993: Implementation of the Arakawa-Schubert cumulus parameterization with a prognostic closure. Prepared for Cumulus Parameterization, a Meteorological Monograph to be published by the American Meteorological Society.

Randall, D.A., Q. Shao, and C.-H. Moeng, 1992: A second-order boundary layer model. J. Atmos. Sci., 49, 1903-1923.

Roberts, R.E., J.E.A. Selby, and L. Biberman, 1976: Infrared continuum absorption by atmospheric water vapor in the 8-12 μm window. Appl. Opt., 5, 2085-2090.

Rockel, B., E. Raschke, and B. Weyres, 1991: A parameterization of broad band raidative transfer properties of water, ice, and mixed clouds. Contr. Atmos. Phys., 64, 1-12.

Rodgers, C.D., 1968: Some extensions and applications of the new random model for molecular band transmission. Quart. J. R. Meteor. Soc., 94, 99-102.

Rutledge, S.A., and P.V. Hobbs, 1983: The mesoscale and microscale structure and organization of clouds and precipitation in midlatitude cyclones. VIII: A model for the "Seeder-Feeder" process in warm-frontal rainbands. J. Atmos. Sci., 40, 1185-1206.

Rutledge, S.A., and P.V. Hobbs, 1984: The mesoscale and microscale structure and organization of clouds and precipitation in midlatitude cyclones . XII: A diagnostic modeling study of precitation development in narrow cold-frontal rainbands. J. Atmos. Sci., 41, 2949-2972.

Stephens, G.L., 1978: Radiation profiles in extended water clouds. Part II: Parameterization schemes. J. Atmos. Sci., 35, 2123-2132.

Suarez, M.J., A. Arakawa, and D.A. Randall 1983: Parameterization of the planetary boundary layer in the UCLA general circulation model: Formulation and results. Mon. Wea. Rev., 111, 2224-2243.

Xu, K-M., and D.A. Randall, 1994: Further development of a cloud parameterization for use in climate models with ARM data. In: Extended Abstracts. Fifth Symposium on Global Change Studies. Nashville, Tennessee, January 23-28, 6-10.